Electronic Supplementary Material (ESI) for RSC Advances.
This journal is © The Royal Society of Chemistry 2022

Electronic Supplementary Information

Stoichiometry-grain size-specific capacitance interrelationships in Nickel Oxide†

Alhad Parashtekar[a,b], Laure Bourgeois[c,d], and Sankara Sarma V Tatiparti[a]*

[a]Department of Energy Science & Engineering, Indian Institute of Technology Bombay, Mumbai 400076, India

[b]IITB-Monash Research Academy, Mumbai, 400076, India

[c]Department of Materials Science and Engineering, Monash University, VIC 3800, Australia

[d] Monash Centre for Electron Microscopy, Monash University, VIC 3800, Australia

***Corresponding author E-mail:** sankara@iitb.ac.in

S1. Grain size estimation

S1a. Williamson-Hall plots

Williamson–Hall method was used to measure the grain size.[1–3] According to Williamson–Hall method, the total peak broadening is given by eqn (1) in the main text.

$$\beta_{hkl} = \frac{K\lambda}{d\cos(\theta)} + 4\varepsilon \tan(\theta) \qquad \text{(1, main text)}$$

Where β_{hkl}: full width at half maximum (FWHM), ε: lattice strain, and d: crystallite length in the direction perpendicular to set of reflecting planes, K: a constant; λ: wavelength of X rays and θ: diffraction angle. The X'Pert Highscore Plus has an in-built function to calculate the grain size using Williamson–Hall method. The in-built function uses eqn (1) (main text) with some rearrangement. In the rearranged equation, eqn (1) is multiplied by $\cos(\theta)$. Then, for all the peaks, $(\beta_{hkl}\cos(\theta))$ is plotted as a function of $\sin(\theta)$. Linear regression was then carried out for this data set. The crystallite length (d) was calculated from the intercept of the best fit line obtained from linear regression. The peaks were fitted with Pseudo-Voigt function to obtain correct FWHM. For the peak fitting, background, specimen displacement, peak position, Cagliotti parameters, and peak shape parameters were refined up to convergence.

The instrument contribution to peak broadening was calculated from the profile fitting of XRD profile of SRM-640 (silicon, shown in Fig. S1).[4] The peak broadening of SRM-640 was entirely attributed to the instrument contribution. The Cagliotti coefficients and Gauss – Lorentzian coefficients, which were calculated from SRM-640, were used as instrument parameters during the profile fitting of other nickel oxide powders. Pseudo-Voigt profile shape was used to model the peaks in diffractogram of SRM-640. The polynomial background function was used for modelling the background. Fig. S1 shows the diffractogram for the SRM-640.

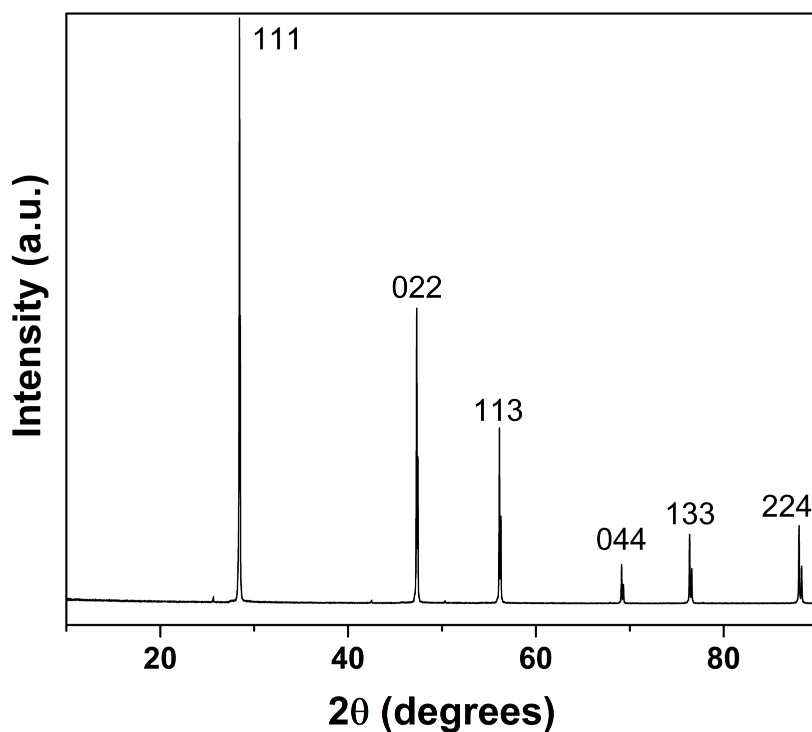

Fig. S1 Powder XRD pattern of SRM-640

The agreement indices for the peak fitting are shown in Table S1.

Table S1: Agreement indices for profile fitting of different nickel oxide powders.

Sample code	Goodness of Fit	Weighted R profile
NiO620	1.11	2.23
NiO720	1.10	2.25
NiO820	1.16	2.36
NiO920	1.19	2.63

Following are the images of Williamson–Hall plots for all the nickel oxide powders generated by the X'pert Highscore software.

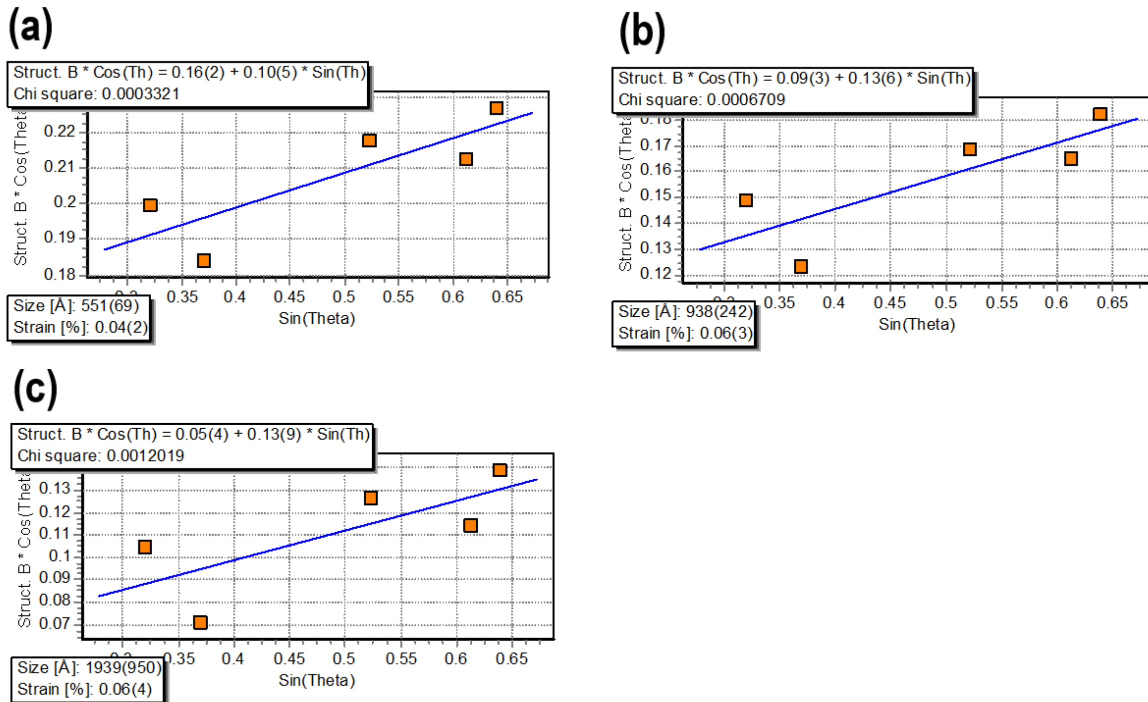

Fig. S2 Williamson-Hall plots for (a) NiO620 (b) NiO720, and (c) NiO920.

S1b. Grain size stability analysis

For checking the grain size stability of the synthesized nickel oxide, X-Ray Diffraction (XRD) was conducted (i) during temperature ramping while reaching the desired temperatures of 620, 720 and 920 ^{o}C and (ii) while isothermal annealing at these temperatures for various durations (5, 10 and 15 h). The XRD patterns during temperature ramping are shown in Fig. S3 and those while isothermal annealing are shown in Fig. S4. The estimated grain sizes during temperature ramping and while isothermal annealing are plotted in Fig. S5.

(i) <u>During temperature ramping</u>

During temperature ramping at 5 ^{o}C/min, detectable nickel oxide starts to form at ~400 ^{o}C. However, the grain size has been estimated through the XRD patterns from 500 ^{o}C onwards, because the patterns at these temperatures show four distinctly visible peaks of nickel oxide which are necessary for using Williamson-Hall method

(see S1a†). The phase evolution and grain coarsening in the nickel oxide can be seen from Figs. S3 and S5. The issue of stability is not relevant for this part of the synthesis as the nickel oxide is being formed in this part.

(ii) *While Isothermal annealing*

From Fig. S5 it can be noticed that the grain size is almost stable while isothermally annealing up to 15 hours at these synthesis temperatures. Since all the studies conducted in this work are on the samples which are annealed for 5 hours, the effect of time is almost negligible on the grain size and the phase evolution. Further, the charge storge experiments were conducted at room temperature. Since the changes in the grain size or phase evolution are negligible while annealing at such high temperatures up to 15 hours, it can be safely assumed that the grain size would be stable even at room temperature.

From the above discussion, the synthesized nickel oxide is considered to be stable in terms of the phase evolution and grain size.

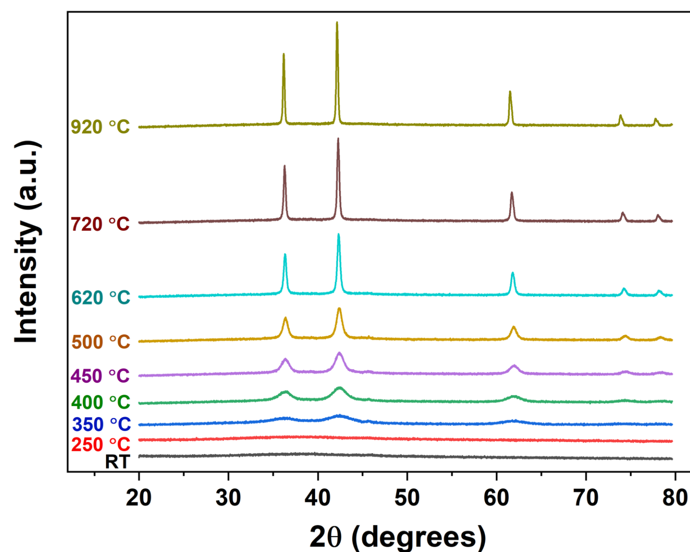

Fig. S3 X-ray diffraction patterns of nickel oxide at different temperatures during synthesis.

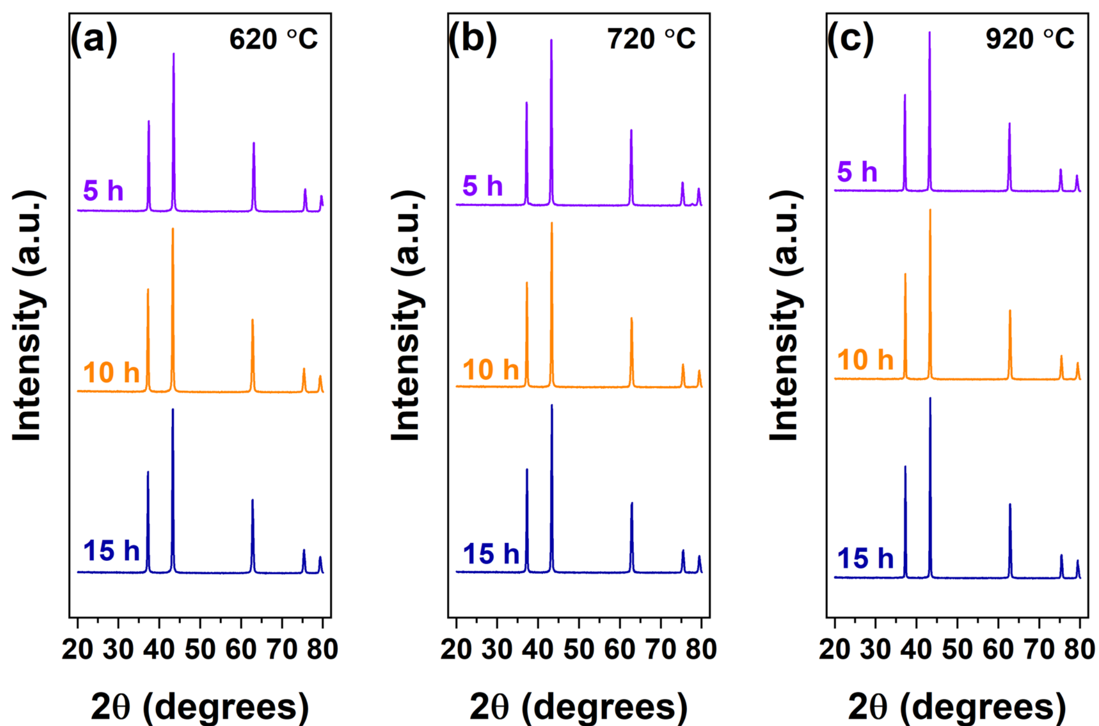

Fig. S4 X-ray diffraction patterns of nickel oxide synthesized at (a) 620, (b) 720 and (c) 920 °C after annealed for 5, 10 and 15 h.

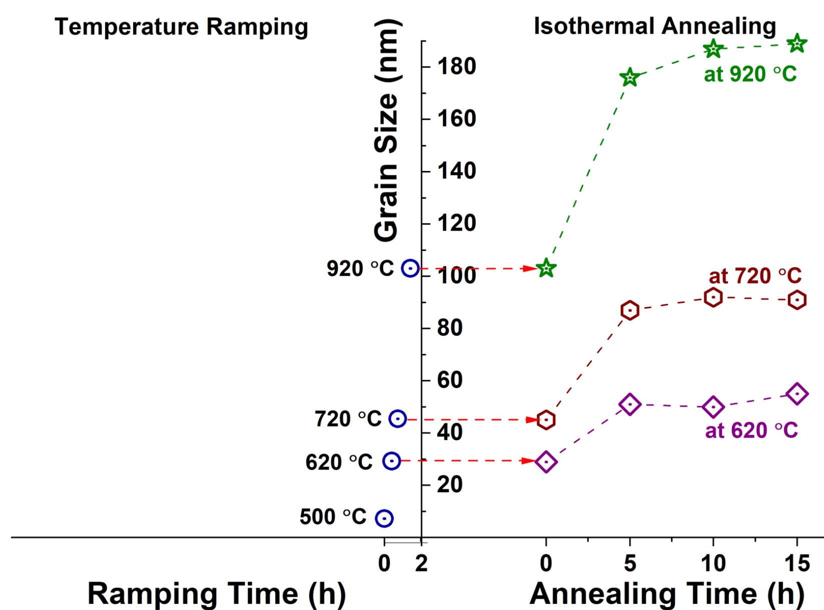

Fig. S5 Grain size variation during temperature ramping while synthesizing nickel oxide and during isothermal annealing at the synthesis temperatures of 620, 720 and 920 °C.

S2. Calculation of mole fraction of Ni^{2+} from x-ray photoelectron spectroscopy[5–7]

The intensity of XPS spectrum for a given sample in the absence of an elastic scattering event is shown in eqn (S1).

$$I = J\ c\ \alpha_{pc}\ K_f \lambda_{IMFP} \tag{S1}$$

Where J is X-ray flux illuminating the sample, c is concentration of electron emitted from the sample volume at fixed binding energy, α_{pc} is photoelectron cross section, K_f is a factor to account for all instrumental effects and λ_{IMPS} is elastic mean free path. I (intensity) in eqn (S1) is the area encapsulated between background and peak under consideration. The product of α_{pc}, K_f and λ_{IMPS} is called relative sensitivity factor (RSF).

Therefore, the ratio $\frac{N_{O^{2-}}}{N_{Ni}}$ using following equation

$$\frac{N_{O^{2-}}}{N_{Ni}} = \frac{I_O/_{RSF_O}}{I_{Ni}/_{RSF_{Ni}}} \tag{S2}$$

The Instrument factor and the amount of flux will cancel out of the equation.

The total yield of photoelectrons from nickel, when its 2p orbital perturbed by photoelectron, is divided into Ni $2p_{3/2}$ and Ni $2p_{1/2}$. Therefore, complete Ni 2p peak is used to calculate I_{Ni}. While I_O was calculated from area under main line in O 1s.

S2a. Calculation of $\frac{N_{Ni^{2+}}}{N_{Ni}}$ from $\frac{N_{O^{2-}}}{N_{Ni}}$:

On dividing eqn (3) (main text), by N_{Ni} we get eqn (S3).

$$2\ \frac{N_{Ni^{2+}}}{N_{Ni}} + 3\ \frac{N_{Ni^{3+}}}{N_{Ni}} = 2\ \frac{N_{O^{2-}}}{N_{Ni}} \tag{S3}$$

By definition of N_{Ni},

$$\frac{N_{Ni^{3+}}}{N_{Ni}} = 1 - \frac{N_{Ni^{2+}}}{N_{Ni}} \tag{S4}$$

On substituting eqn (S4) in eqn (S3), followed by rearrangement eqn (4) (main text) is obtained.

$$\frac{N_{Ni^{2+}}}{N_{Ni}} = 3 - 2 \times \frac{N_{O^{2-}}}{N_{Ni}} \qquad \text{(4, main text)}$$

S2b. Calculation of error in $\frac{N_{Ni^{2+}}}{N_{Ni}}$ ratio:

The error in calculation of $\frac{N_{O^{2-}}}{N_{Ni}}$ is given by eqn (S5).

$$\delta\left(\frac{N_{O^{2-}}}{N_{Ni}}\right) = \sqrt{\left(\frac{\partial\left(\frac{N_{O^{2-}}}{N_{Ni}}\right)}{\partial I_O}\,\delta I_O\right)^2 + \left(\frac{\partial\left(\frac{N_{O^{2-}}}{N_{Ni}}\right)}{\partial I_{Ni}}\,\delta I_{Ni}\right)^2 + \left(\frac{\partial\left(\frac{N_{O^{2-}}}{N_{Ni}}\right)}{\partial RSF_{Ni}}\,\delta RSF_{Ni}\right)^2 + \left(\frac{\partial\left(\frac{N_{O^{2-}}}{N_{Ni}}\right)}{\partial RSF_O}\,\delta RSF_O\right)^2} \tag{S5}$$

On substituting values from eqn 2 (main manuscript) we get eqn (S6).

$$\delta\left(\frac{N_{O^{2-}}}{N_{Ni}}\right) = \sqrt{\left(\frac{RSF_{Ni}}{I_{Ni} \times RSF_O}\,\delta I_O\right)^2 + \left(-\frac{I_O \times RSF_{Ni}}{{I_{Ni}}^2 \times RSF_O}\,\delta I_{Ni}\right)^2 + \left(\frac{I_O}{I_{Ni} \times RSF_O}\,\delta RSF_{Ni}\right)^2 + \left(-\frac{I_O \times RSF_{Ni}}{I_{Ni} \times {RSF_O}^2}\,\delta RSF_O\right)^2} \tag{S6}$$

As no tolerance in RSF values were provided by Kratos, the error in both RSF values was assumed to be 0.05. The area under the O 1s and Ni 2p spectra was calculated by trapezoidal rule. The formula for the trapezoidal rule is shown in eqn (S7).

$$A = \sum_{r=1}^{N-1} \frac{(I_r + I_{r+1})}{2}\,(eV_{r+1} - eV_r) \tag{S7}$$

Here I_r represents the intensity of photoelectrons at binding energy eV_r. N is total number of points recorded. In this case each intensity (I_r) and binding energy value (eV_r) act as a variable. Therefore the total error in calculated area is given by eqn (S8).

$$\delta A = \sqrt{\sum_{r=1}^{n-1} \frac{\partial A}{\partial eV_r}\, \delta eV_r + \sum_{r=1}^{n-1} \frac{\partial A}{\partial I_r}\, \delta I_r} \quad \text{(S8)}$$

There are six types of terms present in eqn (S8) which are given in eqn (S9).

$$\frac{\partial A}{\partial I_1} = \frac{eV_2 - eV_1}{2} \quad \text{(S9a)}$$

$$\frac{\partial A}{\partial eV_1} = \frac{I_2 - I_1}{2} \quad \text{(S9b)}$$

$$\frac{\partial A}{\partial I_n} = \frac{eV_n - eV_{n-1}}{2} \quad \text{(S9c)}$$

$$\frac{\partial A}{\partial eV_n} = \frac{I_n + I_{n+1}}{2} \quad \text{(S9d)}$$

$$\frac{\partial A}{\partial I_r} = \frac{eV_{r+1} - eV_{r-1}}{2} \quad \text{(S9e)}$$

$$\frac{\partial A}{\partial eV_r} = \frac{I_{r-1} - I_{r+1}}{2} \quad \text{(S9f)}$$

On substituting corresponding values in eqn (S9a)-(S9f), the error in the area under XPS spectra was calculated. The error $\frac{N_{O^{2-}}}{N_{Ni}}$ in was estimated by estimating the error in I_O and I_{Ni} by employing eqn (S8) and (S9).

Error in $\frac{N_{O^{2-}}}{N_{Ni}}$ can be used to estimate the error in $\frac{N_{Ni^{2+}}}{N_{Ni}}$ by using condition of global charge neutrality (eqn (4), main text) as shown in eqn (S10).

$$\delta\left(\frac{N_{Ni^{2+}}}{N_{Ni}}\right) = 2 \times \delta\left(\frac{N_{O^{2-}}}{N_{Ni}}\right) \quad \text{(S10)}$$

The derivation of the eqn (S10) is as follows

$$\delta\left(\frac{N_{Ni^{2+}}}{N_{Ni}}\right) = \delta\left(3 - 2 \times \frac{N_{O^{2-}}}{N_{Ni}}\right) \tag{S11}$$

The right-hand side of eqn (S11) reduces to eqn (S12).

$$\delta\left(\frac{N_{Ni^{2+}}}{N_{Ni}}\right) = \delta(3) - \; 2 \times \delta\left(2 \times \frac{N_{O^{2-}}}{N_{Ni}}\right) \tag{S12}$$

In eqn (S12), the error in constant is zero. The error in the ratio has to be absolute, therefore the negative sign is dropped.

S2c. Comparison of O 1s spectrum between freshly synthesized samples and old samples:

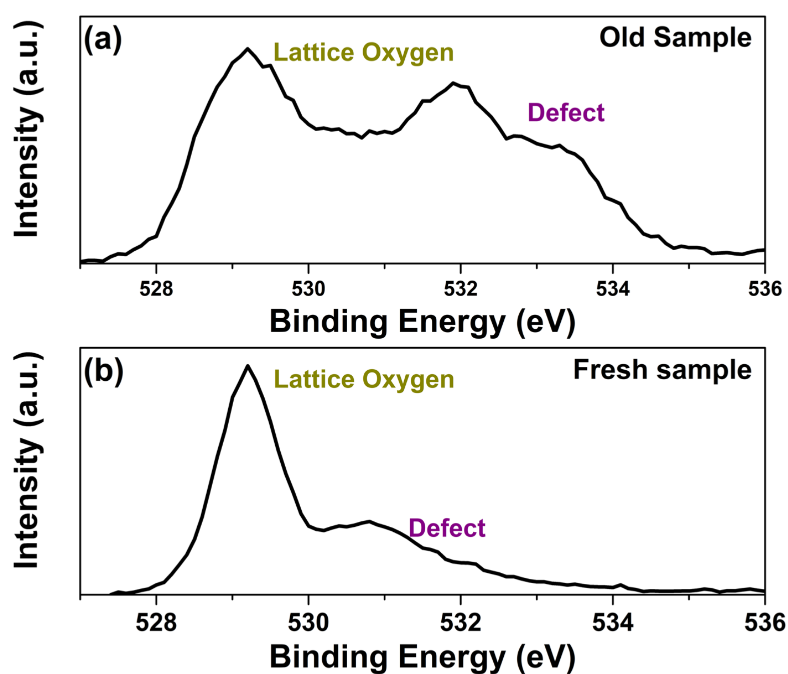

Fig. S6 O 1s XPS spectrum recorded for (a) NiO620 sample synthesized two days prior to XPS scan (b) NiO620 synthesized just before XPS scan.

S3. Cyclic voltammograms of nickel oxide samples

The cyclic voltammetry of nickel oxide was performed in potential range of −0.05 to 0.60 V with respect to Hg/Hg_2Cl_2 reference electrode in 2 M KOH solution. The cyclic voltammetry was performed at different scan rates: 5, 10, 20, 35, 50, 80, 100 mV s^{-1}. Fig. S7 shows the CVs acquired at various scan rates.

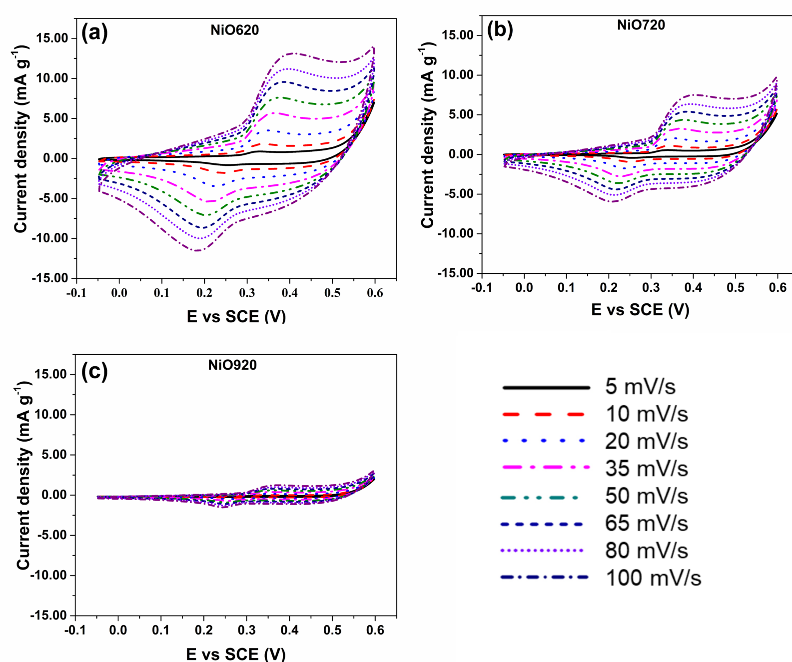

Fig. S7 Cyclic voltammograms of (a) NiO620, (b) NiO720, and (c) NiO920 recorded at different scan rates.

From Fig. S7, both charging and discharging curves exhibit peaks. With an increase in the scan rate, the peak current density increases, and peaks shift towards higher potential in anodic side. This behaviour is a result of the diffusion limited nature of the given redox reaction. With an increase in the scan rate the ion diffusion cannot keep pace with charge transfer.

The specific capacitance was estimated by considering the charging segment of the CV (Fig. 4a, main text). It was assumed that only non-Faradaic processes contributed to current from 0 to +0.25 V. This contribution is almost linear in terms of current density and applied potential,

as can be seen from Fig. 4a (main text). Beyond this potential both non-Faradaic and Faradaic processes contribute to charge storage. The contribution of non-Faradaic processes towards current density beyond +0.25 V followed the same linear relation between current density and applied potential as that up to +0.25 V. The slope and intercept of the line of non-Faradaic current were calculated by linear least-square fitting of CV data from 0 to +0.25 V. Beyond +0.25 V, the current due to the non-Faradic processes was then subtracted from the total current in the CV to obtain the current exclusively from the Faradaic processes. Within this Faradaic segment of the area under CV, the contribution from OH^- adsorption was estimated by truncating the Faradaic segment at ~+0.50 V where the current due to OH^- adsorption is minimal. The remaining part of the Faradaic segment is attributed to the oxygen evolution reaction and is discarded in the present study. The specific capacitance was then calculated mathematically integrating the current density pertaining to the Faradaic part pertaining to OH^- adsorption (i.e. by fixing V_i and V_f in eqn (3) as +0.25 and +0.50, respectively) with respect to time.

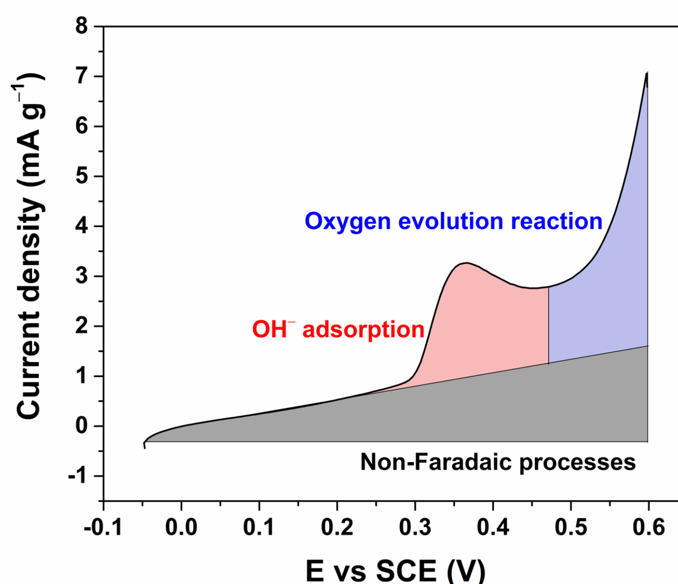

Fig. S8 Schematic representation of division of area under cyclic voltammograms of nickel oxide powders to calculate the contribution of three electrochemical processes in specific capacitance.

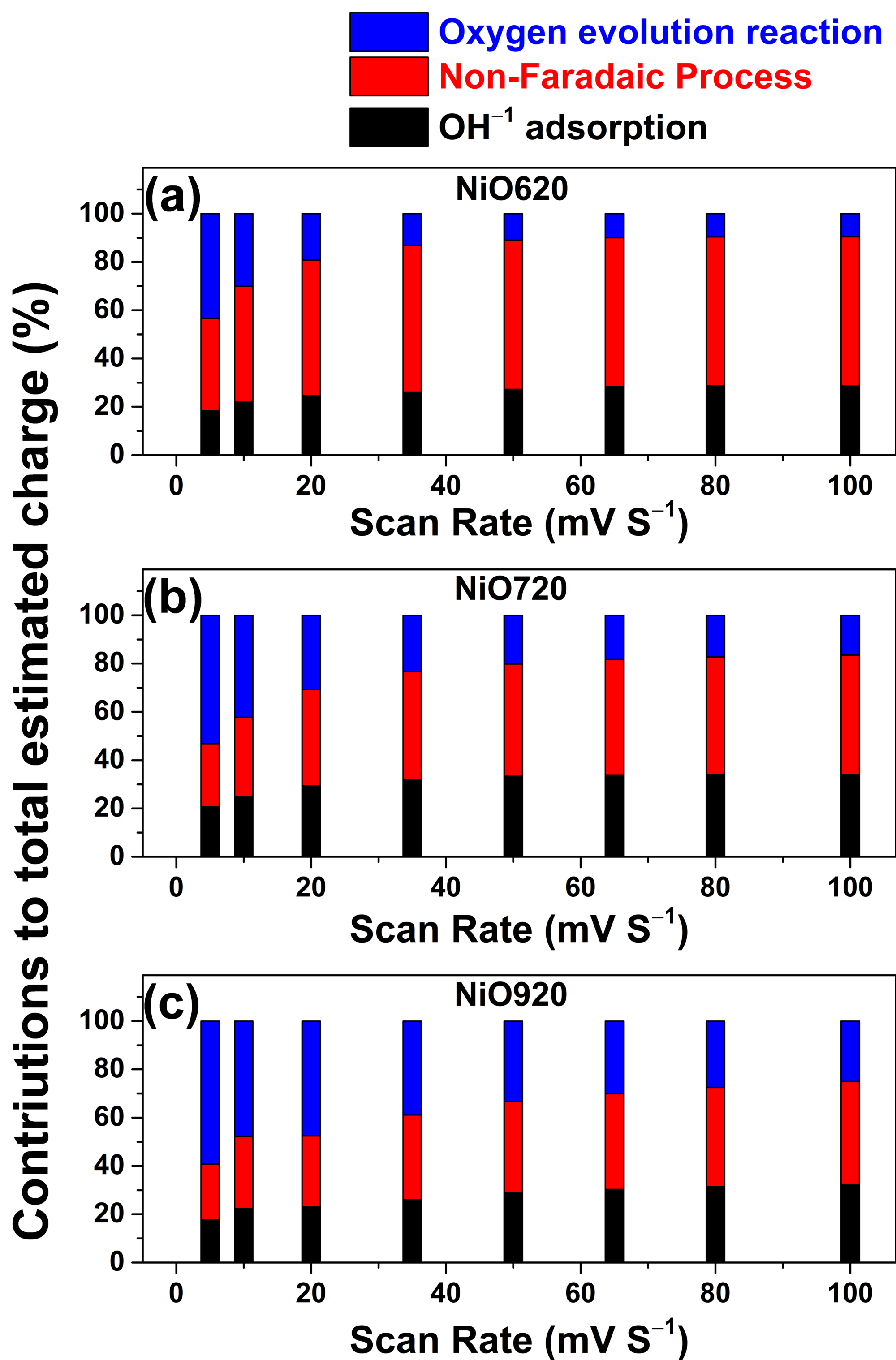

Fig. S9 Contribution of oxygen evolution process, non-Faradaic processes and OH adsorption to total estimated charge as function of scan rate for (a) NiO620, (b) NiO720, and (c) NiO920.

S4. Uncertainty in calculation of specific capacitance and Faradaic contribution

The uncertainties or sources of error in the measurement of specific capacitance can be divided into two subclasses: (i) uncertainty in measurement – random errors because of potentiostat during measurement; (ii) variation in the coating.

The first source of the errors arises from the uncertainty in measuring the current and voltage during cyclic voltammetry. The error in the measurement of each parameter will propagate in the calculation of the specific capacitance. The formula for the specific capacitance is

$$C_{sp} = \frac{1}{w\, v\, \Delta V} \int_{V_i}^{V_f} i\, dV \qquad \text{(6, main text)}$$

Where w is weight if the active material, v is the scan rate and ΔV is voltage window. The uncertainties during measurement incurred due to the least counts of the parameters are listed in Table S2.

Table S2: Least count for different measured entities in eqn 6

Quantity Measured	Uncertainty
Current	1×10^{-5} A
Voltage	0.001 V
Weight	0.0001 g
Scan Rate	0.0001 V/s

The error propagated while computing a function $q(x,y,z,\ldots)$ with $\delta x, \delta y, \delta z \ldots$ as independent and random uncertainties in parameters $x,y,z\ldots$ is given by eqn (S13).

$$\delta q = \sqrt{\left(\frac{\partial q}{\partial x}\,\delta x\right)^2 + \left(\frac{\partial q}{\partial y}\,\delta y\right)^2 + \left(\frac{\partial q}{\partial z}\,\delta z\right)^2 + \cdots} \qquad \text{(S13)}$$

To simplify the calculation of uncertainty in specific capacitance, eqn (6) (main text) can be rewritten as eqn (S14).

$$C_{SP} = \frac{1}{m\, v\, \Delta V} A_{CV} \qquad \text{(S14)}$$

Therefore, the uncertainty in calculation can be calculated using eqn (S15).

$$\delta(C_{SP}) = \sqrt{\left(-\frac{A_{CV}}{m^2 \nu\, \Delta V}\,\delta m\right)^2 + \left(-\frac{A_{CV}}{m\, \nu^2\, \Delta V}\,\delta \nu\right)^2 + \left(-\frac{A_{CV}}{m\, \nu\, \Delta V^2}\,\delta \Delta V\right)^2 + \left(\frac{\delta A_{CV}}{m\, \nu\, \Delta V}\right)^2} \tag{S15}$$

Where, A_{CV} is the term in integration. The 'A_{CV}' was calculated from the discrete numbers of current and voltage values using trapezoidal method for integration. Equation (S16) shows the formula used for computing 'A_{CV}'.

$$A_{CV} = \sum_{i=1}^{n-1} \frac{(C_{i+1}+C_i)}{2}\,(V_{i+1} - V_i) \tag{S16}$$

The same sum can be rewritten in following two ways as shown in eqn (S17) and (S18), when the terms are rearranged.

$$A_{CV} = \frac{1}{2}\left(C_1(V_2 - V_1) + C_n(V_n - V_{n-1}) + \sum_{i=2}^{n-1} C_i(V_{i+1} - V_{i-1})\right) \tag{S17}$$

$$A_{CV} = \frac{1}{2}\left(V_1\,(C_2 - C_1) + V_n\,(C_n + C_{n+1}) + \sum_{i=2}^{n-1} V_i(C_{i-1} - C_{i+1})\right) \tag{S18}$$

The uncertainty in 'A_{CV}' is given by eqn (S19).

$$\delta A_{CV} = \sqrt{\frac{1}{2}\left(\sum_{i=1}^{n}\left(\frac{\partial A}{\partial C_i}\,\delta C_i\right)^2 + \sum_{i=1}^{n}\left(\frac{\partial A}{\partial V_i}\,\delta V_i\right)^2\right)} \tag{S19}$$

The terms in eqn (S19) can be divided into the following six types of terms, as shown in eqn (S 20). In the following equations, the subscript denotes the order of the terms. Subscript 1 indicates the first data point (i.e. beginning of the scan), 'n' indicates the data point corresponding to the highest voltage in the scan, and 'i' subscript represents the rest of the data points.

$$\frac{\partial A_{CV}}{\partial C_1} = (V_2 - V_1) = dV \tag{S20a}$$

$$\frac{\partial A_{CV}}{\partial C_n} = (V_n - V_{n-1}) = dV \tag{S20b}$$

$$\frac{\partial A_{CV}}{\partial C_i} = (V_{i+1} - V_{i-1}) = 2\,dV \tag{S20c}$$

$$\frac{\partial A_{CV}}{\partial V_1} = (C_2 - C_1) \tag{S20d}$$

$$\frac{\partial A_{CV}}{\partial V_1} = (C_2 - C_1) \tag{S20e}$$

$$\frac{\partial A_{CV}}{\partial V_i} = (C_{i-1} - C_{i+1}) \tag{S20f}$$

where dV is voltage step during the scan. On calculating terms given in eqn (S20) and then substituting in eqn (S12) the error in A_{CV} can be obtained. The uncertainty in specific capacitance is shown in Fig. S10. The uncertainty in specific capacitance in percentage was calculated using eqn (S18).

$$uncertainty\ in\ specific\ capacitance\ (\%) = \frac{\delta(C_{SP})}{C_{SP}} \times 100 \tag{S21}$$

To calculate the uncertainty in faradaic contribution, eqn (S13) is used.

$$\delta(\%F) = \sqrt{\left(\frac{\delta A_1}{A_3} \times 100\right)^2 + \left(\frac{A_1}{A_3} \times 100 \times \delta A_3\right)^2} \tag{S22}$$

Where *(%F)* is the uncertainty in contribution of faradaic process in percentage. The uncertainty in A_3 can be calculated directly from CV curve using eqn (S20).

$$\delta A_3 = \sqrt{\left(\frac{-A_{CV}}{\nu^2}\,\delta\nu\right)^2 + \left(\frac{\delta A_{CV}}{\nu}\right)^2} \tag{S23}$$

The uncertainty in A_1 was calculated with same approach directly from equivalent area in the CV curve ($\boldsymbol{A_{gauss}}$). The uncertainty in $\boldsymbol{A_{gauss}}$ was calculated by same approach as that used for the calculation of A_{cv} in eqn (S11). In the case of $\boldsymbol{A_{gauss}}$, the uncertainty in the current was calculated by adding uncertainty due to instrument precision, and error in fitting of Gaussian peak as well as that in the straight line of non-Faradaic current. Errors in the least square fitting

were calculated by computing average of differences between experimental data and fitted curves at each data point. The total uncertainty in current was then calculated by eqn (S24).

$$\delta I = \delta I_{instrument} + \delta I_{gauss} + \delta I_{non-faradaic} \tag{S24}$$

Where δI_{gauss} and $\delta I_{non-faradaic}$ are the average errors calculated for Gaussian peak fit and straight line of non-Faradaic current respectively.

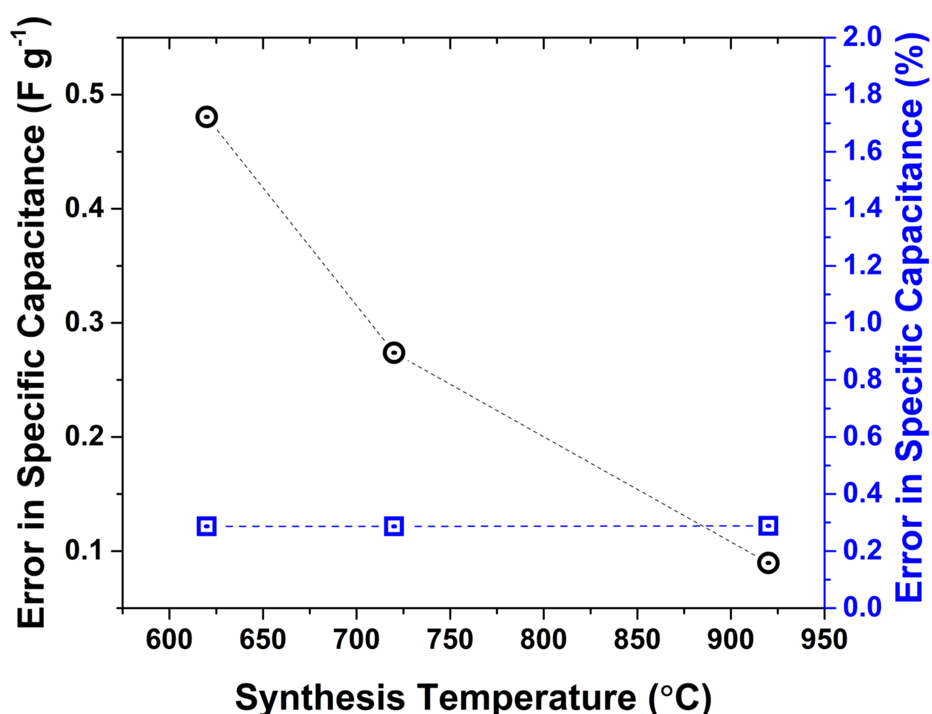

Fig. S10 Propagation error in calculation of the specific capacitance as a function of the synthesis temperature as absolute value and as percentage of estimated value.

S5. Porosity estimation

The porosity was estimated electrochemically from CVs by a method proposed by Trasatti and his co-worker.[8] To measure the porosity, the charge under non-Faradaic portion (+0.25 V) was calculated from the CVs at different scan rates (ν) mentioned in S3†. From these estimated charges (q) and the scan rates two quantities q^{∞} and q^{0} were obtained by linear regression using eqn (S25).

$$q(\nu) = q^{\infty} + k_1\sqrt{1/\nu} \quad \text{(S25a)}$$

$$1/q(\nu) = 1/q^{0} + k_2\sqrt{\nu} \quad \text{(S25b)}$$

Where k_1 and k_2 are constants obtained by regression. The electrochemical porosity (x_{ec}) is then given by eqn 26.

$$x_{ec} = \frac{q^{0}}{q^{\infty} + q^{0}} \quad \text{(S26)}$$

S6. Electrical conductivity estimation

To estimate the electrical conductivity of the samples the nickel oxide powders synthesized at 620, 720 and 920 ^{o}C were pelletized (diameter: 11.5 nm, thickness: 0.4 mm) by compressing them at 8-ton force in hydraulic press followed by annealing at 600 ^{o}C. Electrochemical Impedance Spectroscopy (EIS) was performed on these pelletized powders by employing broadband dielectric analyzer (Concept 80, Novocontrol GmbH, Germany). Prior to performing EIS, silver electrode paste prepared from silver ink mixed with N-butyl acetate was applied on both sides of each pellet. The ink was dried in infra-red lamp for 15 min. A frequency range of 10 to 10^{7} Hz was used to record Nyquist plots on these pellets. The Nyquist plots, as shown in Fig. S11, exhibit distorted semicircle features. The Nyquist plots were used to construct equivalent circuits from which the conductivities of grain and grain boundaries were estimated.

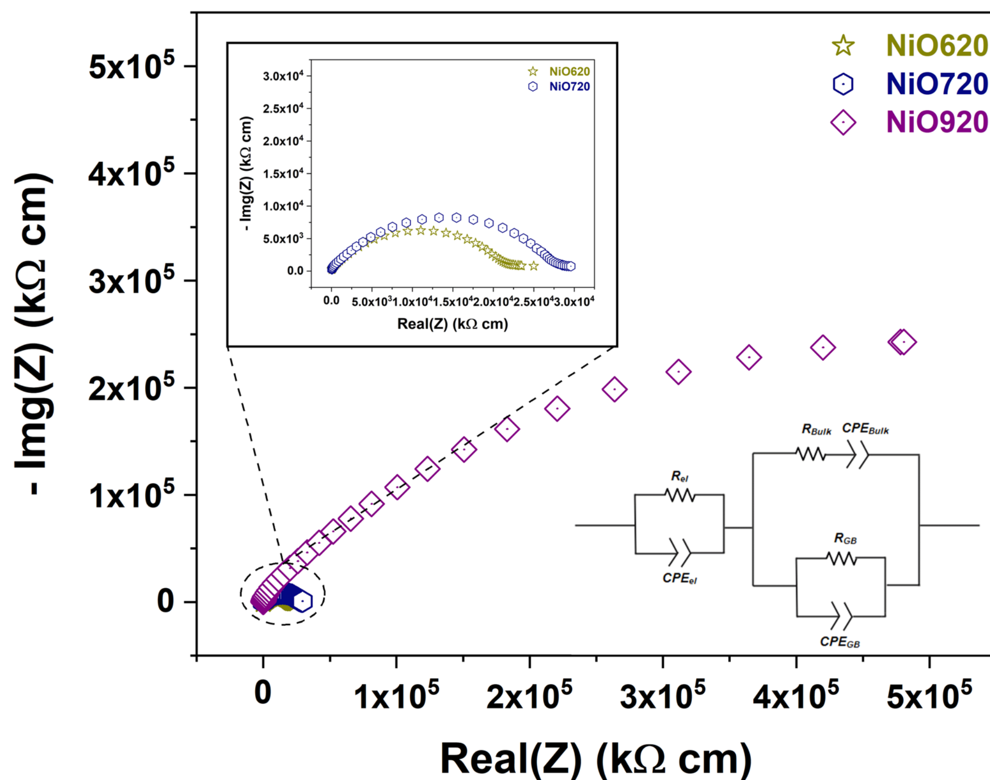

Fig S11. Nyquist plots of the pelletized nickel oxide samples for conductivity estimation.

The corresponding equivalent circuit used for the interpretation of the EIS data is shown in the inset of Fig. S11. In the equivalent circuit R_{el}, R_{Bulk}, and R_{GB} correspond to the resistances offered from the electrode (silver paste), bulk and grain boundary in nickel oxide. The CPE_{el}, CPE_{Bulk}, and CPE_{GB} are the corresponding constant phase elements. Here, CPEs were taken in lieu of pure capacitors as these locally charged regions cannot be modelled as ideal capacitors.[9–12] Values of the various parameters from the equivalent circuit are tabulated in Table S3.

Table S3: The optimized values of various parameters obtained from the equivalent circuit (Fig. S11)

Parameters	NiO620	NiO720	NiO920
R_{el} (ohm-mm)	1.61×10^{-3}	1.63^{-3}	9.1×10^{-3}
Y_{el} (S/mm)	1.57×10^{-8}	3.71×10^{-8}	1.51×10^{-8}
n_{el}	0.99	0.94	0.894
R_{Bulk} (ohm-mm)	5.04×10^{7}	3.95×10^{7}	9.87×10^{10}
Y_{Bulk} (S/mm)	2.31×10^{6}	3.66×10^{6}	1.24×10^{6}
n_{Bulk}	5.70×10^{-1}	5.77×10^{-1}	5.20×10^{-1}
R_{GB} (ohm-mm)	0.097	0.33	2.79×10^{-5}
Y_{GB} (S/mm)	3.81×10^{9}	4.53×10^{9}	1.47×10^{9}
n_{GB}	1	1	0.93

To estimate the conductivity values of grain boundary and bulk region, the conductivity value of any entire sample (i.e. 'global conductivity', here) was estimated from the overall resistance obtained from the equivalent circuit. The global conductivity is plotted as function of synthesis temperature in Fig. S12a. The estimated global conductivities (σ_{Global}, Fig. S12a) of the samples prepared in the present study match with those reported in literature.[13,14] The nominal conductivities of grain boundary and bulk (i.e. σ_{GB} and σ_{Bulk}) were estimated from their respective, estimated resistance values (i.e. R_{GB}, and R_{Bulk}) and the sample dimensions. These values are plotted in Fig. S12b. However, to eliminate dimensional effects from the estimation of conductivities, these nominal conductivities of grain boundary and bulk are divided by the

global value. Such normalized conductivities of grain boundary and bulk (i.e. $\sigma_{GB}/\sigma_{Global}$ and $\sigma_{Bulk}/\sigma_{Global}$) are plotted in Fig. S12c. From Fig. S12b and c, the nominal and the normalized conductivities of the Bulk are almost constant, indicating that the nature of the bulk region of nickel oxide does not change with the synthesis temperature (or stoichiometry, i.e. Ni^{2+}). The nominal and the normalized conductivities of the grain boundary are higher than those of Bulk. This shows that the grain boundaries are more conductive than bulk. Further, the nominal and the normalized conductivities of the grain boundary decrease with synthesis temperature and thus with Ni^{2+} mole fraction. Hence, the higher conductivity near the grain boundaries is a result of the presence of nickel vacancies, and thus, of Ni^{3+} (holes), being consistent with literature.[13,14] Both nickel vacancies and Ni^{3+} provide different conduction mechanisms which are absent in pure nickel oxide containing only Ni^{2+}.[13,14] Such a reduction in the grain boundary conductivity can arise from a decrease in (i) the total grain boundary fraction and/or (ii) Ni^{3+} mole fraction (Fig. 3a) with an increase in synthesis temperature.

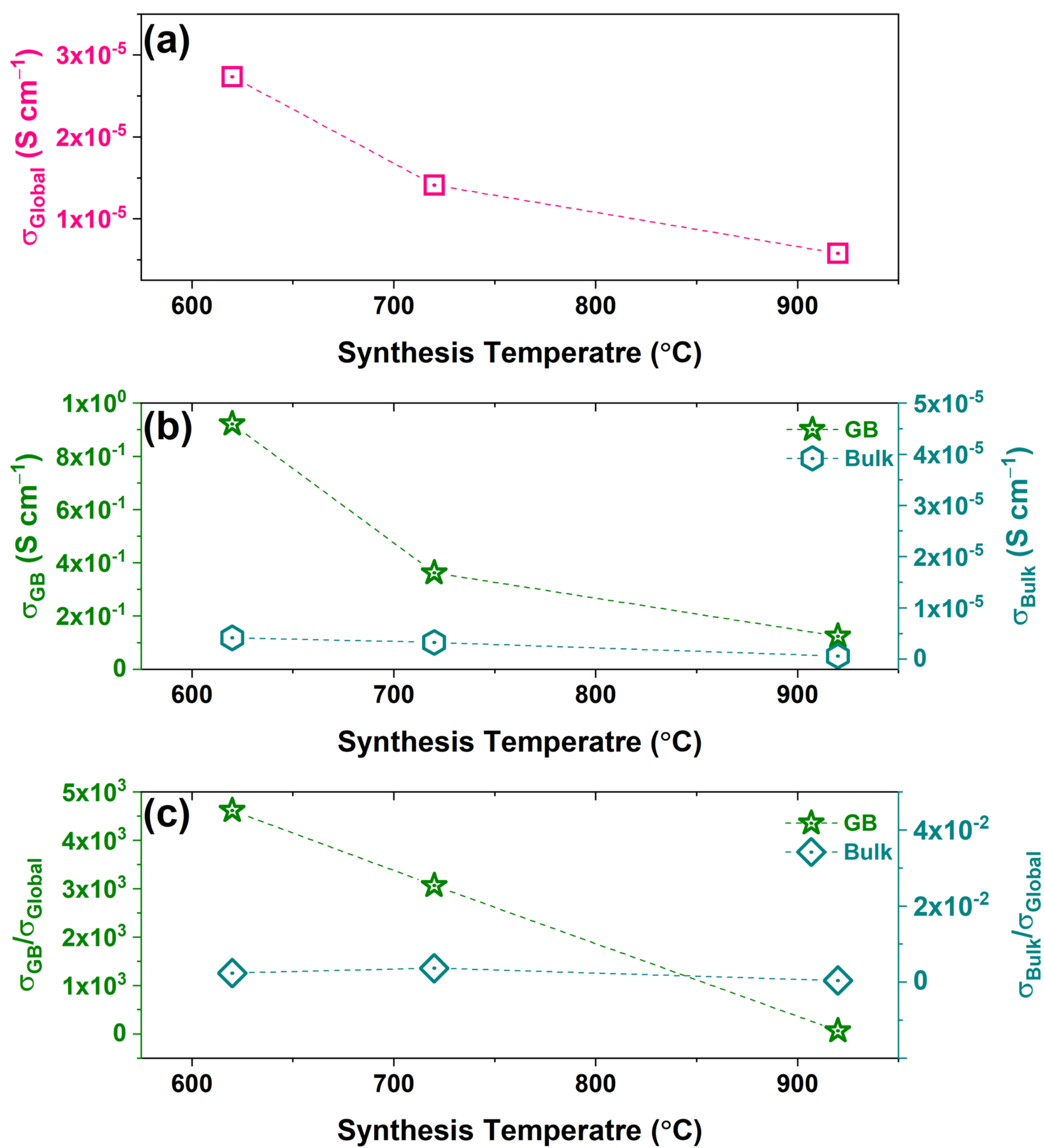

Fig S12. Estimated (a) global conductivity of the entire sample, (b) nominal and (c) normalized conductivities of grain boundary and bulk in nickel oxide synthesized at 620, 720 and 920 ^{o}C.

S7. Thermodynamic Model

S7a. Derivation of Poisson's equation (Eqn (13) in main text)

A set of one grain (Bulk) and one grain boundary (GB) is defined as the system in this model. The location where Bulk and GB join is considered as the interface. The model uses appropriate GB and Bulk sizes as adjustable parameters. The assumptions of the model are: (a) The defects do not interact with each other.[15,16] (b) Formation energy of a given defect is the same everywhere in a given region.[15–17] That is, the likelihood for the presence of the defects is the same everywhere within GB or Bulk, separately. (c) GB and Bulk regions are considered as two separate phases of nickel oxide.[18] (d) The system is treated as thermodynamically open and the exchange of oxygen atoms is allowed between the system and surroundings (eqn (7), main text).

The Gibbs free energy of the system at constant temperature and pressure is given by eqn (S27).[17,19]

$$G = \sum_p \mu_p^{Bulk} n_p^{Bulk} + \sum_p \mu_p^{GB} n_p^{GB} \tag{S27}$$

where, p represents V_{Ni}'', $V_O^{\bullet\bullet}$ and h; μ_p^q: chemical potential of p in region q: Bulk or GB; and n: number of defects in q. The differential change in G is given in eqn (S28).

$$dG = \sum_p \mu_p^{Bulk}\, dn_p^{Bulk} + \sum_p \mu_p^{GB} dn_p^{GB} \tag{S28}$$

At equilibrium,

$$dG = 0 \tag{S29}$$

For the open system (assumption (d)), for eqn (S29) to hold true for any arbitrary change in the number of defects (dn_p^q)[17,18], the chemical potential of every defect should be equal to zero (eqn (S30)).

$$\mu_p^q = 0 \tag{S30}$$

The chemical potential, μ_p^q, as shown in eqn (S31), is the sum of the formation energy of given defect (U_p^q), electrostatic energy $\left(z_p Q \phi(x)\right)$ and configurational entropy $\left(kT \log\left(n_p^q/N\right)\right)$. [17,20]

$$\mu_p^q = \left(U_p^q\right) + \left(z_p Q \phi(x)\right) + \left(kT \log\left(n_p^q/N\right)\right) \tag{S31}$$

where, z_p: net charge on defect, Q: charge on proton, n_p^q: number of p defects per unit volume in q, $\phi(x)$: electrostatic potential, and *N*: number of available sites for defects under consideration in a unit volume. By substitution of μ_p^q from eqn (S31) in eqn (S30) followed by rearrangement, the equation for n_p^q as a function of spatial coordinates (x) in a given region of material (eqn (S32), same as eqn(10) in main text) is obtained.

$$n_p^q = N \exp\left(-\frac{U_p^q + z_p Q \phi(x)}{kT}\right) \tag{S32}$$

In eqn (S32), only electrostatic potential $\phi(x)$ is unknown and is calculated by solving Poisson's equation (eqn (S33), same as eqn (11) in main text). Since, eqn (S33) is applicable to both Bulk and GB, the superscript *q* is omitted.

$$\nabla^2 \phi = \frac{1}{\varepsilon_0}\left(2\,N\,e^{\left(-\frac{U_{V_O^{\bullet\bullet}} + 2\,Q\,\phi(x)}{kT}\right)} + \left(N - N_{V_{Ni}''}\right) e^{\left(-\frac{U_h + Q\,\phi(x)}{kT}\right)} - 2\,N\,e^{\left(-\frac{U_{V_{Ni}''} - 2\,Q\,\phi(x)}{kT}\right)}\right) \tag{S33}$$

where, ε_0: permittivity of vacuum; k: Boltzmann's constant.

S7b. Solution of Poisson's equation (Eqn (S33) or Eqn (11) in main text)

In eqn (S33) *N* is the total number of lattice sites available per unit volume. In order to solve eqn (S33), iterative procedure was employed. One dimensional Poisson's equation was solved separately in bulk and in grain boundary. The sum of the lengths of bulk and grain boundary was maintained equal to the grain size. Potential as a function of distance from GB/Bulk was

found for different initial conditions. Finally, pairs of potential curves, each consisting of potential curves from GB and another potential curve from bulk, were identified such that the overall charge neutrality was maintained according to eqn (S34).

$$Q^{T(GB)} + Q^{T(Bulk)} = 0 \tag{S34}$$

Where Q^T refers to total charge in region that is mentioned in superscript. The value of potential is maximum at GB/Bulk interface which would then approach to the value corresponding to charge neutrality (ϕ_∞) in bulk. The condition of charge neutrality (eqn (S34)) was used to find out ϕ_∞ in GB and in Bulk. The parameter ϕ_∞ was calculated using eqn (S32). The charge neutrality in any given region as given in eqn (8) in main text is expanded as eqn (S35).

$$(N - N_{V_{Ni}''}) * \exp\left(-1 * \frac{U_h + Q\phi_\infty}{kT}\right) + 2N * \exp\left(-1 * \frac{U_{V_O^{\bullet\bullet}} + 2Q\phi_\infty}{kT}\right) = N * \exp\left(-1 * \frac{U_{V_{Ni}''} - 2Q\phi_\infty}{kT}\right) \tag{S35}$$

As the first step of computation, Poisson's equation was written in 1 dimension as shown in eqn (S36).

$$\frac{d^2\phi}{dx^2} = \frac{-Q}{\varepsilon_0}\left(2\,N\,e^{\left(-\frac{U_{V_O^{\bullet\bullet}} + 2\,Q\,\phi(x)}{kT}\right)} + (N - N_{V_{Ni}''})\,e^{\left(-\frac{U_h + Q\,\phi(x)}{kT}\right)} - 2\,N\,e^{\left(-\frac{U_{V_{Ni}''} - 2\,Q\,\phi(x)}{kT}\right)}\right) \tag{S36}$$

By using substitution $\left(\psi = {d\phi}/{dx}\right)$, eqn (S36) can be reduced to variable separable form

$$\psi\,d\psi = f(\phi)\,d\phi \tag{S37}$$

On integrating eqn (S37) and further rearrangement eqn (S38) can be obtained.

$$\frac{d\phi}{dx} = \pm \left(\frac{2\,N\,kT}{\epsilon\,\epsilon_r} \left(e^{-\left(\frac{U_h}{k_B T}\right)}\, e^{-\left(\frac{Q\,\phi}{k_B T}\right)} + e^{-\left(\frac{U_{V''_{Ni}}}{k_B T}\right)}\, e^{+\left(\frac{2\,Q\,\phi}{k_B T}\right)} + e^{-\left(\frac{U_{V_O^{\bullet\bullet}}}{k_B T}\right)}\, e^{-\left(\frac{2\,Q\,\phi}{k_B T}\right)} - e^{-\left(\frac{U_{V''_{Ni}}}{k_B T}\right)}\, e^{-\left(\frac{U_h}{k_B T}\right)}\, e^{\left(\frac{Q\,\phi}{k_B T}\right)} \right) - const \right)^{1/2} \tag{S38}$$

Equation (S38) is a first order autonomous differential equation. Therefore, the slope of the solution is only dependent on potential value at the position. Since the potential has to be constant once it reaches its ϕ_∞, the constant was calculated such that ${d\phi}/_{dx} = 0$ when $\phi = \phi_\infty$. The constants of integrations are different for Bulk and GB regions. Since GB is negatively charged and space charge zone has net positive charge, the right hand side of eqn (S38) is negative for GB region and positive for bulk region. The equations were solved for a range of starting potentials (initial conditions) ϕ_∞.

S7c. Formation Energies

The formation energy of point defects in nickel oxide were calculated by several research groups. Duffy and Tasker calculated the energy of the vacancy by considering the nickel oxide crystal without any defects as the reference state. Other researchers have calculated the formation energy of nickel vacancy with Fermi level as the reference.[21–27] The formation energy values with respect to the pure crystal was used to calculate the concentration of the defects.[28] In nickel oxide, the nickel vacancies have higher formation energy in bulk when compared to different the grain boundaries.[29] However, the values of the formation energy calculated by Duffy and Tasker are higher than 22 eV.[29] These values result in zero vacancy concentration ($\sim 10^{-350}$ m^{-3}). The experiments carried out by Haugsrud et al. show that the concentration of the nickel vacancies as fraction of total number of nickel ions is 3×10^{-4} at

1200 °C.[30] The calculation of formation energy using eqn (S39) gives the formation energy value to be 1.09 eV.

$$n_{defect} = N_{defect}\, e^{-\left(\frac{\Delta E_{defect}}{2kT}\right)} \tag{S39}$$

Bruemmer et al. also reported experimental values of nickel vacancy to be near 1.5 eV.[24] Both these observations suggest that the formation energy of the nickel vacancy is between 1 – 2 eV. The formation energy of holes as calculated by Duffy and Tasker is more than 30 eV [29], which results in the concentration of holes as zero. Their calculation showed that the formation energy of the holes is less in bulk than that in the grain boundary. Duffy and Tasker have not considered oxygen vacancies for the analysis.[29] The formation energy of oxygen vacancy is reported by Bruemmer et al. as 2.5 eV.[24] Due to the unavailability of the formation energies of the defects, here we considered the general relation between the formation energies of the three defects in the range of 0 – 2 eV.: 1) in bulk – ($U_h < U_{V_{Ni}} < U_{V_O}$) 2) in grain boundary – ($U_{V_{Ni}} < U_h < U_{V_O}$).

Table S4: Formation Energies of Defects[24]

Region	Defect	Formation Energy (eV)
Grain Boundary	Nickel Vacancy	1.0
	Oxygen Vacancy	2.5
	Hole	1.5
Bulk	Nickel Vacancy	1.5
	Oxygen Vacancy	2.5
	Hole	1.0

References

1. M. Kahouli, A. Barhoumi, A. Bouzid, A. Al-Hajry and S. Guermazi, *Superlattices Microstruct.*, 2015, **85**, 7–23.
2. A. Seetharaman and S. Dhanuskodi, *Spectrochim. Acta - Part A Mol. Biomol. Spectrosc.*, 2014, **127**, 543–549.
3. P. Scardi, M. Leoni and R. Delhez, *J. Appl. Crystallogr.*, 2004, **37**, 381–390.
4. E. J. Sonneveld, G. J. M. Sprong, T. H. De Keijser and R. Delhez, *Powder Diffr.*, 1995, **10**, 129–139.
5. M. C. Biesinger, B. P. Payne, L. W. M. Lau, A. Gerson and R. S. C. Smart, *Surf. Interface Anal.*, 2009, **41**, 324–332.
6. B. P. Payne, M. C. Biesinger and N. S. McIntyre, *J. Electron Spectros. Relat. Phenomena*, 2012, **185**, 159–166.
7. A. G. Shard, *J. Vac. Sci. Technol. A*, 2020, **38**, 041201.
8. S. Ardizzone, G. Fregonara and S. Trasatti, *Electrochim. Acta*, 1990, **35**, 263–267.
9. J. Liang and Y. Li, *Ceram. Int.*, 2019, **45**, 14153–14159.
10. A. V. Kuzmin, S. S. Plekhanov and A. S. Lesnichyova, *Electrochim. Acta*, 2020, **348**, 136327.
11. M. Takahashi, Y. Noguchi and M. Miyayama, *Solid State Ionics*, 2004, **172**, 325–329.
12. V. V. Kharton, A. L. Shaula, N. P. Vyshatko and F. M. B. Marques, *Electrochim. Acta*, 2003, **48**, 1817–1828.
13. V. Biju and M. Abdul Khadar, *J. Mater. Sci.*, 2001, **36**, 5779–5787.
14. S. S. Nair and M. A. Khadar, *Sci. Technol. Adv. Mater.*, 2008, **9**, 21–33.
15. D. M. Duffy and P. W. Tasker, *Philos. Mag. A*, 1985, **50**, 143–154.
16. D. M. Duffy and P. W. Tasker, *Philos. Mag. A*, 1983, **48**, 155–162.
17. R. A. De Souza, *Phys. Chem. Chem. Phys.*, 2009, **11**, 3010.
18. R. Kirchheim, *Acta Mater.*, 2002, **50**, 413–419.
19. D. M. Duffy and P. W. Tasker, *Philos. Mag. A*, 1987, **50**, 143–154.
20. D. R. Franceschetti, *Solid State Ionics*, 1981, **2**, 39–42.
21. W. B. Zhang, N. Yu, W. Y. Yu and B. Y. Tang, *Eur. Phys. J. B*, 2008, **64**, 153–158.
22. J. Osorio-Guillén, S. Lany and A. Zunger, *AIP Conf. Proc.*, 2009, **1199**, 128–129.
23. Z. Sun, Y. Zhao, M. He, L. Gu, C. Ma, K. Jin, D. Zhao, N. Luo, Q. Zhang, N. Wang, W. Duan and C. W. Nan, *ACS Appl. Mater. Interfaces*, 2016, **8**, 11583–11591.
24. J. Yu, K. M. Rosso and S. M. Bruemmer, *J. Phys. Chem. C*, 2012, **116**, 1948–1954.
25. S. Lany, J. Osorio-Guillén and A. Zunger, *Phys. Rev. B*, 2007, **75**, 1–4.

26 N. Alidoust and E. A. Carter, *Phys. Chem. Chem. Phys.*, 2015, **17**, 18098–18110.

27 J. Rabier, J. Soullard and M. P. Puls, *Philos. Mag. A*, 1990, **61**, 99–108.

28 C. B. Carter and G. Norton, in *Ceramic Materials*, 2013, pp. 253–274.

29 D. M. Duffy and P. W. Tasker, *Philos. Mag. A Phys.* 1982, **50**, 143–154.

30 R. Haugsrud and T. Norby, *Solid State Ionics*, 1998, **111**, 323–332.